Microdissected tumor cuboids: a microscale cancer model that retains a complex tumor microenvironment

Lisa F Horowitz[1#], Ricard Rodriguez-Mias[2], SongLi Zhu [3], Noah R Gottshall[1], Ivan Stepanov[1,4], Casey Stiles[1], Marcus Yeung[3], Tran NH Nguyen[1,5], Ethan J Lockhart[1], Raymond S Yeung[6], Judit Villen[2], Taranjit S Gujral[3], and Albert Folch[1]

[1] Department of Bioengineering, University of Washington, Seattle, WA, USA.
[2] Department of Genome Sciences, University of Washington, Seattle, WA, USA.
[3] Human Biology Division, Fred Hutchinson Cancer Research Center, Seattle, WA, USA.
[4] Department of Mechanical Engineering, University of Washington, Seattle, WA, USA.
[5] Department of Biochemistry, University of Washington, Seattle, WA, USA.
[6] Department of Surgery, University of Washington, Seattle, WA, USA.
[#] Email: lisafh@uw.edu

ABSTRACT

Present cancer disease models – typically based on cell cultures and animal models that lack the human tumor microenvironment (TME) – are extremely poor predictors of human disease outcomes. Microscale cancer models that combine the micromanipulation of tissues and fluids offer the exciting possibility of miniaturizing the drug testing workflow, enabling inexpensive, more efficient tests of high clinical biomimicry that maximize the use of scarce human tissue and minimize animal testing. Critically, these microscale models allow for precisely addressing the impact of the structural features of the heterogeneous TME to properly target and understand the contributions of these unique zones to therapeutic response. We have recently developed a precision slicing method that yields large numbers of cuboidal micro-tissues ("cuboids", ~ $(400\ \mu m)^3$) from a single tumor biopsy. Here we evaluate cuboids from syngeneic mouse tumor models and human tumors, which contain native immune cells, as models for drug and immunotherapy evaluation. We characterize relevant TME parameters, such as their cellular architecture (immune cells and vasculature), cytokine secretion, proteomics profiles, and their response to drug panels in multi-well arrays. Despite the cutting procedure and the time spent in culture (up to 7 days), the cuboids display strong functional responses such as cytokine and drug responses. Overall, our results suggest that cuboids make an excellent model for applications that require the TME, such as immunotherapy drug evaluations, including for clinical trials and personalized oncology approaches.

INTRODUCTION

Cancer drug testing – a central process in cancer drug development, personalized oncology, and cancer disease research models – is often inaccurate and inefficient because it typically relies on studies in cell cultures or animals that lack the human tumor microenvironment (TME).[1] In the last decade, functional drug testing technologies such as patient-derived organoids[2] (PDOs) (also termed "tumor spheroids") and organs-on-chips[3] (OOCs) have revealed the power and clinical relevance of *ex vivo* testing of cancer patient tissue. However, in these platforms, which often take weeks to months to establish, the tumor tissue is generated *de novo* by growing the patient's cancer cells.[4] Critically, PDOs and OOCs can only test effects on the tumor cells themselves because the rest of the TME, including the immune microenvironment, is lost during the process of tissue growth and/or expansion in culture – limiting their relevance as models for immunotherapy since many immunotherapy drugs act on the TME.[5–7] These limitations are a fundamental hurdle for the personalization of therapies which need to be customized to the unique TME of the patient,[8] and also for the development of combination immunotherapies, which often target the human TME.[9] Only <4% of cancer drugs out of the ~1,000 drugs in clinical trials each year pass the safety and efficacy tests;[10] more than half of the failures are due to lack of efficacy.[11] Due to this inefficiency, the average drug takes >10 years to come to market at a total cost of >$1 billion.[12] The pace of progress in

clinical studies puts an additional pressure to developing reliable drug efficacy tests: immunotherapy clinical trials, especially in combination with other therapies, are exponentially rising in number.[13]

In addition to PDOs and OOCs, several other functional approaches to drug testing have been proposed, each with advantages and limitations. Implantable or needle microdelivery devices[14,15] locally deliver small doses of (up to 16) drugs to the tumor *in vivo,* with maximal preservation of the TME, but issues of tumor accessibility and patient safety limit their applicability. PDX mouse models permit the study of drug responses in an intact organism,[16] however in PDXs most of the TME is from the host mouse and PDX from individual patients grow too slow to inform initial post-operative therapeutic decisions.

Micro-dissected tumors ("µDTs"), also termed "*ex vivo* tumor fragments", are a spheroid approach that has been used for decades to preserve the tumor and its TME (with its native immune cells) within manually-cut small (~1-3 mm-wide) pieces.[17–21] µDTs have shown promise for the study of immunotherapy with checkpoint inhibitors, but at very low throughput.[22–27] The µDTs are minced manually with a scalpel and grown in collagen gel either on Transwells[25–27] or in microchannels.[23,24] Astolfi et al. prepared ~420 µm-diam. cylindrical µDTs by punching cores from PDX tumor slices and manually loading them in microchannels with five traps each; the reproducible size of the µDTs allowed for a metabolite transport model.[28] Since, at the time of intervention, most tumors are only a few centimeters wide[29] (and the improvement in early detection techniques[30] keeps reducing the tumor sizes), we have developed a microdissection technique that generates large numbers of µDTs while preserving the TME. The technique is based on mechanically cutting tumors with a tissue chopper into thousands of regularly-sized, cuboidal-shaped µDTs (referred to as "cuboids") in ~30 min.[31] Theoretically (if the blade were infinitely thin and did not cause tissue loss), a ~1 cm^3 cube of solid tumor would yield 15,625 400 µm-wide cuboids, or 62,500 250 µm-wide cuboids. In practice, from an irregular ~1 cm^3 tumor piece we obtain thousands of ~400 µm-wide cuboids and more than 10,000 ~250 µm-wide cuboids, with some loss from the cutting process.

Here we provide an extensive characterization of cuboids from mouse and human tumors to illustrate the retention and function of the native TME over several days in culture. We evaluate the presence of immune cells and vasculature, and demonstrate responses of the immune cells by cytokine secretion assays. In addition to traditional tissue culture platforms, we utilize devices with microfluidic arrays that facilitate 3D imaging and analysis as well as drug testing. In addition to traditional viability drug responses, we probe deeper into drug responses by protein profiling of signaling pathways and by proteomics. In a single assay, proteomics provides a complex readout that encompasses molecular responses to drugs as well as profiling the TME, including immune cells and cytokines. These support cuboids as an ideal live cancer model system with a rich TME and suitable for a wide variety of tools to deeply investigate cancers in the context of their TME.

RESULTS

Evaluation of cuboids in culture

As shown schematically in **Figure 1**A, we can perform a variety of analytical and functional assays on regularly-sized micro-dissected tissues, or "cuboids", cultured in traditional well plates or in custom microfluidically arrayed miniature wells. We generated two sizes of cuboids (250 or 400 µm)^3 from mouse or human tumors (**Fig. 1**B)[31]. We first prepared tumor slices either with a vibratome (250 or 400 µm)^3 or with a tissue chopper (400 mm).^{3} For experiments with mouse cuboids with an intact immune system, we used mouse syngeneic breast cancer tumors derived from the Py8119 cell line grown subcutaneously or orthotopically in the mammary fat pad. Py8119 tumors bear similarity to triple-negative breast cancer [ref]. The cuboid's shape changed from polygonal immediately after cutting, to rounded by the following day. Live/dead staining at day 3 (**Fig. 1**B,C) showed viability of ~90% for both sizes of cuboids (average without outliers). We approximated the cuboid sizes at day 3, when they were rounded, by a diameter

estimated from their area from an image (**Fig. 1**C). The mean diameter for the 250 µm cuboids was 313 µm (287 and 330, 25% and 75% quartiles), and for the 400 µm cuboids, it was 426 µm (262 and 451), with much of the variability likely due to the observed variations in the thickness of the initial slice. A vibratome provides more control and precise thickness of slices. We chose to continue with the 400 µm size as a compromise between representation of the TME and nutrient exchange. Each 400 µm cuboid has approximately 4.1 times more volume (and thus TME) than the smaller 250 µm cuboid. Further increases in size would result in hypoperfused cores.[32] As seen in tumor slices before cutting into cuboids (**Fig. 1**B,D), patient tumor (colorectal cancer metastatic to the liver, CRCm) has more heterogeneity with non-tumor stromal regions and necrotic bloody regions than the mouse syngeneic breast cancer model does.

Mouse cuboid TME

We next evaluated how the TME of Py8119 mouse breast cancer cuboids evolved over a week in culture. Although tissue explants can be grown for longer periods[ref], we focused on first week in culture, long enough for the functional assays but not longer to minimize the time in which the inevitable remodeling of the tumor and its TME occurs. To evaluate the TME at a cellular level, we performed 5-plex multi-immunohistochemistry (multi-IHC) on thin sections of 400 µm cuboids cultured in suspension in well plates up to a week in culture (**Fig. 1**E), with quantitation by HALO (**Fig. 1**F). Comparison of day 0 to day 3 in culture showed general maintenance of tissue structure by H&E, followed by shrinkage of the spheroids by day 7, potentially secondary to apoptosis of the central core. Apoptotic cell death (cleaved-caspase 3, CC3) was minimal initially, limited to necrotic regions from the initial tumor seen at day 0, a few scattered cells the subsequent days, and often in the central region at day 3 (~10% of the cells), and decreased in the smaller sized cuboids of day 7. Proliferation (Ki-67) started very high initially, with ~50% of cells at day 0 and 45% at day 1, gradually reduced to ~25% at day 3, but still persisted with ~10% at day 7. Endothelial cell staining (CD31) gradually diminished from ~0.4% of the total area at day 0, to half at day 3, then to minimal staining at day 7. Staining for tumor cells (CK19) was weak and variable so was not used for quantitation (data not shown). Staining for immune cells (CD45) was strong initially then gradually diminished, and was variable between tumors, ranging from 10-60% of the cells at day 0. As shown in graphs (**Fig. 1**F), similar staining was seen in Py8119 tumors grown subcutaneously or orthotopically in the mammary fat pad (n=2 and 3, respectively).

To look at specific immune cell types present in the cultured cuboids, we performed an additional 5-plex mIHC of near adjacent cuboid sections (**Fig. 1**E,F). Like in Py8119 slices in culture by flow analysis,[33] in cuboids by multi-IHC we found that tumor-associated macrophage (TAMs) were the most frequent, comprising ~10% of the total cells throughout the week in culture. There were also many tumor associated neutrophils (Lys6G), though with weaker staining. We also observed scattered T cells (CD3) including some CD8+ T cells. We didn't see many natural killer cells (NKp46) in the cuboids, which is consistent with the few clusters of positive cells seen in sections of the initial tumor. With multi-IHC we quantitated the average amount multiple immune cell types and endothelial cells for single 2D planes of groups of multiple cuboids and not for individual cuboids, given the scarcity of sampling per cuboid and the small size of cuboids, especially relevant for the rarer cell types. Despite these limitations, the immunostaining clearly revealed the continued complexity of the cellular microenvironment in cuboids over short term culture.

Patient cuboid heterogeneity

We also looked at cuboids derived from patient liver tumors. In contrast to the relatively homogeneous mouse tumor models such as the Py8119 breast cancer tumors above, patient tumors are known to display large amounts of heterogeneity, both within tumors and between tumors of the same type. As seen in a patient colorectal cancer liver metastasis (CRCm; **Fig. 1**G), thin sections of the initial tumor, and

of cuboids before and after culture in 6-well plates, also clearly showed great variability in histology (H&E). We had previously found in colorectal cancer liver metastases (CRCm) that regions of autofluorescence and darkness on brightfield corresponded to relatively acellular stromal regions, presumably due to post-necrotic fibrosis after neoadjuvant treatment.[34] With the CRCm cuboids we found that we could identify putative stromal cuboids by brighter autofluorescence in the green channel, and bloody cuboids (red in light) as relatively dark areas in the green channel (**Fig. S1**). To evaluate viability, we measured viability by RealTime-Glo luminescence after 1 day and saw a correlation with identification as stroma by autofluorescence. Similarly, we saw a correlation between low RTG viability and stromal histology with H&E in cuboids from another patient CRCm, cultured in collagen with an air-liquid interface in transwell inserts (**Fig. S1**). Importantly, although heterogeneity of patient tissue requires evaluation of more cuboids per condition, use of individual cuboids could be a tool to capture heterogeneity of patient tumor responses.

Distribution of immune and endothelial cells between mouse cuboids

To evaluate the distribution and heterogeneity of immune and endothelial cells among individual cuboids, we performed 3D immunostaining and analysis of intact mouse Py8119 cuboids (**Fig. 2**). We evaluated immune cells by CD45 and endothelial cells by CD31 of cuboids cultured in microtrap arrays that facilitated immunostaining, clearing, and confocal analysis. The small microfluidic device contained 3 wells, each with one outlet connected to 48 traps (145 traps total) (**Fig 2**A,B). To load the device using fluid flow, cuboids suspended in viscous 20% PEG were moved in bulk along the surface with a plastic sheet while applying rapid liquid suction (200 mL/hr). We loaded one well/outlet at a time, resulting in 1-3 cuboids per trap in approximately one min. The cuboids were then cultured, fixed, immunostained, cleared, and imaged on the device. Subcutaneous and orthotopic cuboids from day 0 and day 2 were immunostained with CD45 for immune cells and with CD31 for endothelial cells (**Fig. 2**C). 3D visualization and analysis of immunostained surfaces with Imaris revealed abundant CD45 cells, and persistent CD31 vasculature, though reduced and becoming more sparse (**Fig. 3**D). Quantitation of the amount of endothelial CD31 (**Fig. 3**E,F) reveals the increase in variability between cuboids from day 0 to day 2, with most of the decrease happening in the larger cuboids (**Fig. 3**F). In contrast, although there was an overall decrease in the amount of immune cell CD45 staining at day 2, there was not a difference based on cuboid size (**Fig. 3**E,F).

3D immunostaining of patient cuboids

For patient cancer cuboids, we performed similar 3D immunostaining experiments that looked at CD45+ immune cells and at CC3+ apoptotic cells, given the larger amount of starting cell death compared to mouse. For day 0 cuboids, we looked at 1 CRCm and 1 idiopathic cholangiocarcinoma (ICC) tumor (**Fig. 2**G,H). CRCm cuboids were manually loaded onto a microtrap device after fixation, while the ICC cuboids were microfluidically loaded onto a microtrap device (96 traps connected to one outlet) for culture and staining, with one cuboid per trap. In contrast to the relatively homogenous makeup of the day 0 cuboids from the mouse breast cancer model, the patient cuboids were markedly more heterogeneous, including in the amount of tumor (regions with many nuclei) versus non-tumor tissue (regions with very few nuclei). Similarly, the CD45+ immune cells were present variably and in clusters. While with mouse cuboids, we saw minimal initial cell death, aided by elimination of necrotic areas during preparation, with patient cuboids we saw multiple regions of cell death, as seen in day 0 cuboids within cuboids (**Fig. 2**G,H), as well as the presence of multiple cuboids without many cells (**Fig. S1**). Analysis of staining at day 4 of the ICC revealed continued presence of CD45+ immune cells, and some increase in CC3+ apopototic cells. Concurrent viability measurements with RealTime-glo luminescence confirmed the viability of the cuboids

(**Fig. S1**). The immunostaining results reinforce the observation that patient versus mouse tumor cuboids show increased heterogeneity in tumor representation, in immune cell distribution, and in presence of dead cells prior to culture. The immunostaining also confirms at the whole cuboid level the continued presence of immune cells in culture seen by multi-IHC.

Immune cell cytokine and chemokine secretion in cuboids

To evaluate the functionality of the immune cells within the cultured cuboids, we measured cytokines/chemokines in mouse and human cuboids grown in U-bottom 96-well plates with multiple cuboids per well (**Fig. 3**). Luminex measurement revealed abundant expression of cytokines/chemokines in the supernatant of Py8119 breast cancer and MC38 colon cancer cuboids, with 15 detected for Py8119, and 29 for MC38 (**Fig. 3**A,B). For Py8119, expression of multiple molecules secreted by the innate immune system (e.g. G-CSF, IL-6, and TNFα) is consistent with the abundant macrophage seen in cuboids by immunostaining above. CXCL10 may be produced by monocytes, endothelial cells, and fibroblasts. The interferon-gamma (IFNg) signal is consistent with the presence of T cells in cuboids by immunostaining. In MC38 cuboids, 25 of the cytokine/chemokines were present at >10 pg/mL. Application of lipopolysaccharide (LPS) to stimulate the innate immune system led to the expected increases in inflammatory cytokines, IL-1α and TNFα, and chemokines CCL3, 4, and 5 (**Fig. 3**C). For human cuboids, we also looked at the supernatant from cuboids prepared from a patient colorectal cancer liver metastasis (**Fig. 3**D). We observed 5 different cytokine/chemokines, supporting the presence of functional immune cells such as macrophage in the cuboids. CXCL-10 has been shown to be expressed by CRC tumor cells as well as by macrophage. IL-8 is a key pro-inflammatory pro-tumor chemokine produced by tumor cells and tumor-associated macrophage in CRC.[35] CCL2 and CCL5 can be produced by CRCm tumor cells themselves.[36] CCL18 is produced by macrophages and monocytes. These cytokines support the use of cuboids as a model system in which cells express cytokines/chemokines critical to the immunomodulatory crosstalk between tumor and immune cells.

Variability of the drug response with cuboids

As a first demonstration of drug responses in mouse cuboids, we treated Py8119 cuboids from a subcutaneous mouse breast cancer with 2 drugs using a 24-well device with 96 microfluidic traps, one device per condition (**Fig. 4**A-H). Each microfluidic trap contained up to 3 cuboids, with 4 traps per well. We measured viability by RealTime-Glo (RTG) luminescence on an IVIS machine before and after 3 day treatment with the cytotoxic chemotherapy drug, cisplatin; the non-specific protein kinase inhibitor, staurosporine, as a positive control; or a no drug negative control. The separation of the cuboid traps on the device in an array facilitated analysis of viability by luminescence for individual traps, immobilizing cuboids in fixed location. We observed significant responses to both CP and STS. Similar responses were seen using a Py8119 tumor grown orthotopically, using a device with three regions of 48 traps each (**Fig. S2**). While these microfluidic devices don't allow for multiple different drug treatments in fluidically connected wells, we have also added traps to a 96-well version of the microtrap device (Lockhart et al., submitted).

To look at the variability of the drug response at the level of individual cuboids, in parallel on the same tumor we tested individual cuboids, manually pipetted into a 384-well plate (**Fig.4**I-M). As in the microdevice, we saw a strong decrease in viability (RTG) in response to cisplatin and staurosporine. We also saw an increase in cell death using a green fluorescent cell death marker, SYTOX Green (SG). Despite the relative homogeneity of the tumor, there was some heterogeneity in the viability before drug treatment and in the viability after culture for the control conditions. For these drugs, power analysis

showed that to detect a 50% change, we would need 2 cuboids for SG and 5 for RTG, and to detect a 30% change, we would need 4 cuboids for SG and 12 cuboids for RTG. These experiments were performed on the relatively homogenous mouse Py8119 tumor, so we expect that the number of cuboids needed for each condition with more heterogenous tumors, especially with human patient tumors, would be much greater.

We then performed similar experiments on cuboids from a patient's colorectal cancer metastasis to the liver (**Fig. 4**N-U). The patient had undergone chemotherapy prior to resection, including only one cycle with FOLFOX (folinic acid, 5FU, and oxaliplatin) because of side effects. As seen in tumor slices (**Fig. 1**D) and cuboids (**Fig S1**), the tumor had regions that correspond to relatively acellular stroma as described before,[34] likely due to post-treatment necrosis. These regions looked lighter with top-illumination, dark with through illumination, and brighter with green autofluorescence. Also visible were regions with blood that were red with top illumination, dark with through illumination, and very dark with green autofluorescence. We note that the same regions may also contain tumor cell areas, as the slices and cuboids were regularly thick (400 mm), and they may be quite interspersed, as seen on H&E (**Fig. 1**G). We used a custom robot pipet to pipet 1 cuboid per well of a 384 well plate. For viability, we measured RealTime-Glo luminescence before drug application on day 2, then after drug application on days 5 and 7. We treated cuboids with either the standard chemotherapy regimens FOLFOX or FOLFIRI (5-fluorouracil and irinotecan), or staurosporine, or DMSO vehicle control, or a no drug control. As an additional cell death readout, we measured cell death with propidium iodide (PI), a red nuclear cell death indicator, at the end of the experiment on day 7. Pretreatment viability was variable, but similar between the wells used for the different treatments (**Fig. S1**). We observed both a decrease in viability and an increase in cell death at day 7 to FOLFOX, FOLFIRI, and staurosporine, consistent with the patient's relative lack of prior exposure to FOLFIRI and FOLFOX, which are the first line choices for treatment.[37,38] The responses were highly significant despite the clear heterogeneity in the baseline signal, in the changes to control and DMSO treatments over time, and in the drug responses.

Cuboid responses to drug panels

To demonstrate the suitability of cuboids for drug screening, we tested a drug panel of kinase inhibitors on mouse Py8119 cuboids in a standard 96-well plate format (**Fig. 5**). We manually pipetted a random number of cuboids into each well, which resulted in 2-6 cuboids per well. After measuring the pretreatment viability by RTG luminescence, we removed high and low luminescence outliers in order to reduce the variability of the starting condition. We measured the drug responses (post/pre) after 3 days of drug treatment, relative to the DMSO vehicle control. The relatively high concentration used (1 µM) may contribute to the responses to many of the tested drugs. The relative reproducibility of the responses for duplicate wells for Py8119 breast cancer cuboids for this experiment contrasts with the variability seen in the single cuboid experiments with the same tumor type. We attribute this difference to both the use of a pool of cuboids per well here, as well as to only including the wells with more similar starting luminescence in the treatment phase. The combination of multiple cuboids per well presents to be a good strategy to reduce noise and to minimize reagent use for higher throughput drug testing approaches.

Profiling changes in signaling pathways from drug treated mouse cuboids.

We then used reverse-phase protein array (RPPA) to look at dynamic changes in signaling pathways in mouse cuboids with drug treatment (**Fig. 6**). Py8119 breast cancer cuboids were probed with antibodies to look at the activity of 48 proteins, primarily by the phosphorylation state of kinases. Cuboids were treated with cisplatin (10 and 100 µM), doxorubicin (an anthracycline cytotoxic chemotherapy drug, 10

μM), staurosporine (2 μM), or DMSO vehicle control. Two samples of ~10 cuboids each were probed with 48 antibodies, and 23 yielded high-quality signals. The corresponding 23 proteins revealed distinct protein correlations, physical and predicted functional protein-protein interactions, and enriched biological processes from gene enrichment analysis. Six proteins of interest showed differences between drug treatments and DMSO (**Fig. 6**A,B). Phospho-histone H2A.X (P-H2A.X), a marker of DNA damage, is elevated in the drug treatments relative to controls, as expected. A dramatic reduction in pERK signal was seen for all drug treatments. Reductions in p-CREB, p-S6rp(S240/244) and p-SFK varied between drugs, with staurosporine and the higher cisplatin concentration causing greater decreases than doxorubicin or than the lower cisplatin concentration. Results from the 23 proteins of interest were used to create a Pearson correlation matrix and a protein-protein interaction network (**Fig. 6**C,D). Finally, gene enrichment analysis of the positively correlated proteins (**Fig. 6**E) yielded the top biological processes involved: regulation of apoptosis, transmembrane receptor protein tyrosine kinase signaling pathway, regulation of telomerase activity, and regulation of telomere maintenance. Thus, RPPA can provide a rich, targeted analysis of dynamic changes in signaling pathways in cuboids in response to treatments.

Proteomics of drug-treated mouse cuboids.

In order to provide a deep molecular readout of both drug-induced changes and the state of the TME at once, we developed a method for proteomic analysis of cuboids (**Fig. 7**). We treated cuboids from Py8119 orthotopic mouse breast cancer tumors in 6 well plates for 3 days with several drugs including kinase inhibitors. Treatments included the drugs clinically used for cancer: cisplatin (100 μM), paclitaxel (a cytotoxic chemotherapy microtubule inhibitor; 10 μM), and crenolanib (a PDGFR inhibitor; 0.5 μM), and regorafenib (a VEGFR inhibitor; 0.5 μM); as well as doramapimod (a pan p38 MAPK inhibitor used for some autoimmune diseases; 0.5 μM) and a DMSO (0.1%) vehicle control. We prepared samples from replicates of 4 cuboids each, including no treatment (day 4) and pretreatment (day 1) controls. The data independent acquisition (DIA) strategy consistently identified over 50000 precursors and 4000 proteins per sample across treatments using the equivalent of 1 cuboid per injection (**Fig. S3**A). The DIA strategy also afforded precise protein quantifications (median CV<10%) across drug treatments (**Fig. S3**B), which resulted in high Pearson correlations across the dataset (>0.95)**.**

Analysis of the expression of select cancer and TME-relevant proteins from day 1 cuboids demonstrated the ability of the one proteomics assay to reveal similar information as other assays such as immunostaining, viability, and cytokine, but with types of markers at once (**Fig. 7**A,B). Among others, we saw multiple proteins involved in cytokine and chemokine activities (**Fig. 7**A) as well as several tumor microenvironment markers (**Fig. 7**B). These tumor microenvironment markers included proliferation (Ki67) and apoptosis (CC3), key measures of drug response; AGRE1 (F4/80) and CD68, markers of macrophage; MRC1 (CD206), a marker of M2 macrophage; PTPRC (CD45) a general marker for immune cells; and VME (vimentin), a marker for tumor cells and the epithelial-mesenchymal transition. Although this approach does not have the cellular resolution of immunostaining or the sensitivity of Luminex cytokine measures, it can in one test evaluate death, proliferation, cell types, and signaling using many target proteins.

We also examined the effects of the different drugs on the cuboid proteome. Clustering analysis (**Fig. 7**E) and protein abundance Pearson correlations across replicates (**Fig. 7**C), revealed that cuboid proteomes undergo substantial and reproducible remodeling in response to drug treatments. Paclitaxel treatment seems to elicit the most dramatic proteome changes in cuboids as reflected by the cluster separation in the PCA analysis (**Fig. 7**E). Crenolib appeared to cause changes in the proteome relative to DMSO, but to a smaller extent. A closer look at the cytotoxic microtubule inhibitor Paclitaxel identified expected patterns of drug action, with decreased proteins related to actomyosin structural reorganization and upregulation of proteins related to activation of the innate immune system (**Fig.7**D). Gene Ontolology

enrichment analysis (**Fig.7**F) of regulated genes between DMSO or Paclitaxel treated samples also identified additional significantly regulated biological processes.

CONCLUSION

Here we presented multiple approaches that supported the use of micro-dissected tissue "cuboids" as an *ex* vivo live tumor model for functional drug testing and cancer biology. Multi-IHC of mouse cuboids over a week in culture revealed continued proliferation and persistence of key cell types including immune cells. 3D immunostaining of endothelial and immune cells showed the heterogeneity of the cuboids. Cytokine secretion from mouse and human cuboids further supported the functionality of the immune cells in cuboids. Drug treatment of individual mouse and human cuboids demonstrated the amount of heterogeneity in the responses by both viability and cell death assays, while treatment of cuboids in groups facilitated testing a drug panel. With RPPA on mouse cuboids we showed molecular profiling of the signaling pathways in response to drugs. Finally, we demonstrate the power of proteomic analysis of mouse cuboids to deeply analyze molecular changes in response to drugs, as well as to reveal the presence and functional state of the tumor microenvironment. Together, this data supports the potential for this cuboid system and other intact tissue µDT's to help bridge the critical gap for cancer biology and cancer drug testing between organoids, which have high throughput and lack TME, and human patients. Cuboids offer higher throughput than patient slices, while preserving much of the TME, unlike organoids. The possibility to integrate cuboids with many modalities of assays will allow researchers to tailor experiments with cuboids to help tackle outstanding problems in cancer biology and treatment.

MATERIALS AND METHODS

Cell culture

The Py8119 syngeneic mouse breast adenocarcinoma cell line (American Type Culture Collection (ATCC), CRL 3278) was grown in DMEM/F12 (for subcutaneous injection) or F-12K (for orthotopic injection) supplemented with 5% FBS and 1% penicillin/streptomycin. The MC38 syngeneic mouse colon carcinoma cell line (Kerafast, ENH204-FP) was cultured in DMEM supplemented with 10% FBS and 1% penicillin/streptomycin. Tissue culture reagents were obtained from GIBCO, ATCC, or Fisher.

Tumor generation for mouse model

Mice were handled in accordance with institutional guidelines and under protocols approved by the Animal Care and Use Committee at the University of Washington, Seattle or by the Fred Hutchinson Cancer Research Center. Mouse syngeneic tumor cell lines (Py8119 and MC38) were injected into C57BL mice (Jackson Laboratories), >6 week old female (Py8119) or male (MC38) mice. 1-2 x 10^6 cells were injected subcutaneously (both lines) or orthotopically in Matrigel (Py8119, Corning). Tumors were harvested at < 2 cm^3. If not used immediately, the tumor was stored up to overnight in Belzer-UW cold storage medium (Bridge-to-Life Ltd).

Human tissue

Human tissue was obtained with written informed consent and treated in accordance with Institutional Review Board approved protocols at the University of Washington, Seattle. Colorectal cancer liver metastases (CRC) and intrahepatic cholangiocarcinoma were processed for sliceing the same day as the resection. CRC3: Biopsy from a 40 year-old male with metastatic colorectal carcinoma to the liver, responsive to neoadjuvant treatment. Slices were cultured overnight after the biopsy and made into cuboids (considered as day 0). Cuboids were grown in 1 mL of collagen on a transwell with an air liquid

interface and analyzed for viability and drug response using RealTime-Glo (Promega), followed by immunostaining. CRC6: Biopsy from a 43 year-old male with colorectal carcinoma metastatic to the liver, after being off chemotherapy for a year. Cuboids were cultured in a 96 well plate, followed by immunostaining and imaging in the microfluidic device. ICC-2: Biopsy from a 70 year-old female with untreated intrahepatic cholangiocarcinoma. Cuboids were cultured in microwell devices, followed by immunostaining and imaging in the device. CRC8: Biopsy from a 29 year-old female with rectal cancer with recurrent metastasis to the liver, after initial treatment with CAPOX (capecitabine and oxaliplatin) followed by only one cycle of FOLFOX 2 months. Slices were cultured overnight and cuboids were prepared the following day. Cuboids were either grown in a 6-well plate for multi-IHC, or placed individually into a 384-well plate for drug treatment using a custom pipetting robot [Gottshall et al. 2024-biorxiv].

Cuboid generation and culture

After removing necrotic region from the tumors, we generated cuboids as previously described.[31] For human tumors, and if specified for mouse tumors, slices were cut using a Leica VT 1200 S vibrating microtome or MZ5100 vibratome (Lafayette Instruments) after embedding tissue punches (600 mm diameter, Harris Uni-Core) in 1-2% lo-melt agarose. Otherwise, we cut small pieces of tissue into slices using a tissue chopper (McIlwain) after attaching the tissue to the plastic disk with cyanoacrylate glue. We cut slices into cuboids with the tissue chopper, then gently dissociated the cuboids with a transfer pipette. For 400 µm cuboids, we filtered them for size less than the 750 µm filter and greater than a 300 µm filter (Pluriselect). To further remove potential contamination, we transferred the cuboids to a 100 µm cell strainer (Corning or Falcon) and passed them 2 times through sterile PBS and once with medium. For the scarce human tumors, we did these washes in sterile tubes instead. For CRC and ICC human cuboids, MC38 mouse cuboids, and Py8119 cuboids (cytokine, checkpoint inhibitor, and drug panel experiments), the culture medium was HFH: Williams' Media E (Sigma) supplemented with nicotinamide (12 mM), L-ascorbic acid 2-phosphate (50 mg/mL), D-(+)-glucose (5 mg/mL) from Sigma; sodium bicarbonate (2.5%), HEPES (20 mmol/L), sodium pyruvate (1 mM), Glutamax (1%), and penicillin–streptomycin (0.4%) from Gibco; and ITS + Premix (1%) and human EGF (20 ng/mL) from BD Biosciences. For other Py8119 experiments (e.g. immunostaining, RPPA, and proteomics), cuboid culture medium was DMEM/F12 with 5% heat-inactivated fetal bovine serum, penicillin-streptomycin (0.1%). One human colorectal cancer tumor (CRC3) was cultured in 1 mL collagen on top of a 0.4 µm filter Transwell PFTE membrane insert (PICMORG50, Millipore) in 6 well plates, with 1.3 mL culture medium placed below. We prepared 80% collagen (Corning rat tail collagen type 1, 354236, 3-4 mg/mL) with 10 % 10x PBS, and 10% serum-free medium. We then used filtered-sterilized 1M NaOH to neutralize the pH to ~7.2.

Drug treatment of cuboids

To measure viability, RealTime-Glo (Promega) was added at 1x or 0.5x and after overnight incubation, the baseline luminescence was read by IVIS (Perkin-Elmer). Drug was added to the well, and luminescence was read again after incubation with drug without further addition of RealTime-Glo. To measure cell death as an endpoint, SYTOX green (1/50,000; Invitrogen), propidium iodide (1 µg/mL), and/or Hoechst (16 µM, Invitrogen) were added to the well, incubated 1 hr at 37°C, then imaged with or without washing twice in PBS. For drug panel experiments, multiple cuboids were randomly pipetted manually, and baseline viability was used to remove outliers before randomly assigning treatments.

The 35 drug panel for treatment of Py8119 cuboids, in order, was DMSO, Baricitinib (LY3009104, INCB028050), Doramapimod, JNK Inhibitor VIII, TCS ERK 11e (ERK Inhibitor VIII, VX-11e), Rho Kinase Inhibitor III Rockout, PP121, GZD824, Staurosporine, AZD3463, NVP-BVU972, Y-39983 dihydrochloride, Cobimetinib, WZ3146, Aminopurvalanol A, SB202190 (FHPI), PD 166285 dihydrochloride, BIIB-057 (PRT062607, P505-15), Akt Inhibitor VIII Isozyme Selective Akti-1/2, CP 547,632, Bosutinib, AT7867,

Cdk1/2 Inhibitor III, PDK1/Akt/Flt Dual Pathway Inhibitor, SB 218078, PF-3644022, LY 333531 mesylate (Ruboxistaurin), Cot inhibitor-2, PD 173955 Analogue 1, Vargatef (Nintedanib), BIBF 1120), K252a, Nilotinib, GSK650, Regorafenib, Pazopanib, and At9283. Drugs were obtained from MedChemExpress, Selleckchem, TOCRIS, Cayman, and Sigma.

Microfluidic device fabrication and use

Microchannels were made in a process adapted from Horowitz et al.[31] We designed the devices in AutoCAD (Autodesk), and then fabricated them by laser micromachining (VLS3.60, Scottsdale, USA) of PMMA substrates followed by thermal solvent bonding and adhesive bonding. The device has four layers. The 800 µm-thick PMMA channel network layer (Clarex, Astra Products) has laser-cut microchannels that connect the outflow channel(s) to microtraps via binaries. The microtraps were approximately 560 µm in diameter at the top and 620 µm at the bottom. The microchannels were approximately 410 µm wide except for near the traps where they were approximately 320 µm wide. After sonication of the microchannel layer in isopropanol for 1 min, we bonded it to a 300 µm-thick PMMA sealing layer (Clarex, Astra Products) using thermal solvent bonding; we exposed both layers to chloroform vapor (~3 mm above the liquid) for 4 min, manually pressed them together, then sealed in a heat press for 5 min at 140 degrees, 240-260 psi. The well plate layer was laser-cut from 6.35 mm-thick PMMA (1227T569, McMaster-Carr, Elmhurst, IL) and bonded to the channel layer using double-sided 3M™ High-Strength Acrylic Adhesive 300LSE for 2 min at 250 psi in the thermal press. Silicone tubing was bonded to the outlets using cyanoacrylate glue. Optionally, an additional well plate layer was hand bonded onto the device after cuboid loading using the 300 LSE. The devices were sterilized by running 70% ethanol through the channels.

To load cuboids into the devices, cuboids were suspended in ice cold 20% polyethylene glycol (8k-PEG P2139, Sigma-Aldrich) and pipetted into the well. Suction was applied with a 60 cc syringe and a syringe pump (Chemyx Inc.) at 200 mL/h for 96-microtrap wells or 100 mL/h for 48-microtrap wells. Mouse cuboids were pushed around the well slowly using either a custom window (single well, 96 trap device), or a comb (3 well device). For the scarce human cuboids, under visualization with a VHX-970F microscope (Keyence), cuboids were pushed manually to the vicinity of the traps using forceps to encourage only one cuboid per trap. More PEG and more cuboids were loaded as needed. The loading process took about 10 min for the 96-trap wells and 1 min for each 48-trap well. The device was placed into a 10 cm petri dish for culture.

Immunostaining and histology

For multi-immunohistochemistry experiments, tissue pieces and cuboids were fixed in 4% paraformaldehyde and washed with PBS. Cuboids were then embedded in Histogel (Epredia) plugs. Tissue was then processed for microarrays, paraffin sectioning, hematoxylin & eosin (H&E) staining, and multi-immunohistochemistry (multi-IHC) by the Experimental Histopathology Service at the Fred Hutchinson Cancer Research Center. Paraffin section (4 µm) were stained using the X machine/process X/Y with either two five-plex (mouse) or three three-plex (human) stains. Lists of antibodies are given in the supplemental materials. DAPI was used as a nuclear counterstain.

For peroxidase immunostaining (**Fig. S1**), tissue was fixed in 4% paraformaldehyde overnight then cryoprotected with 30% sucrose/PBS overnight two times. Cryosections (14 µm thickness) were then processed for H&E or for immunostaining. For immunostaining, we pretreated with 0.6% hydrogen peroxide in methanol for 30 min, washed, and then performed antigen retrieval by steaming for 30 min in 10 mM sodium citrate, 0.05% Tween 20 (Sigma), pH 6.0. After at least 30-min block in blocking solution (Tris-NaCl-blocking buffer or TNB buffer, Perkin Elmer, with 0.1% Triton X-100), we incubated the tissues

with rabbit primary antibodies (diluted in TNB) overnight at 4°C. Antibodies were: active cleaved caspase 3 (1/600, Cell Signaling), Ki-67 (1/1,000, AbCAM, ab15580), CD31 (1/200, AbCAM ab28364), or CD45 (1/1,000, AbCAM, ab10558). After incubation of the tissues with an anti-rabbit peroxidase polymer (Vector Labs MP7401) for 30 min, we visualized the staining with 3,3'-Diaminobenzidine (DAB, Vector Labs) and a light hematoxylin counterstain. Washes between steps were done with PBS except for just before DAB incubation, done with 10 mM Tris pH 7.5.

We performed whole mount immunostaining in the microfluidic devices with a protocol adapted from Li et al.[39] Cuboids were incubated in block (PBS + 0.3% Triton + 1% BSA + 1% normal mouse serum) for >12 hrs at 37°C on a shaker, then in primary antibody diluted in block for 2 days at 37°C on a shaker. Primary antibodies were Alexa 647 anti-mouse CD45 (1:200; Biolegend), Alexa 488 anti-mouse CD31 (1:250; Biolegend), Alexa 647 anti-human CD45 (1:400; HI30 Biolegend 304056), rabbit anti-human/mouse cleaved-caspase 3 (1:300; Cell Signaling, 9661). followed by 1:500 546-Donkey/Goat anti-rabbit (or other). We then washed the cuboids 3 times with PBS at least 8 hrs total at 37°C on a shaker. For the unlabeled primary we incubated with Alexa 546 donkey anti-rabbit IgG (1:500; Invitrogen) diluted in block for 2 days at 37°C on a shaker followed by washing as above. DAPI 1 µg/mL was added to the last antibody step. We then cleared the tissue by incubation in previously prepared Ce3D solution overnight at room temperature with shaking. The day 0 human ICC cuboids were immunostained in a centrifuge tube and imaged in a custom well.

Imaging and image analysis

We took images using a Canon DS126601 on a Nikon SMZ1000 dissecting scope, a Nikon Eclipse Ti microscope, a BZ-X800 (Keyence) microscope, or a Leica SP8 confocal microscope (10x, 2 µm Z steps). For general image manipulation we used FIJI.[40]

For multi-IHC image analysis, we used HALO and HALO Link (Indica Labs). For cellular analyses, cells were identified by nuclear DAPI stain, then cytoplasmic boundaries were drawn. We antibodies with clear staining, we applied the same settings to all tissues (Ki-67, CD45, CD3, CD8, and F4/80). For NKp46 which had few cells in cuboids d1-d7 with high background, we did a manual count. For Ly6G, we used one setting for strong staining and another for the groups of cuboids with high background. For area analyses, we applied the same settings to all tissues of that tumor type. We used the background staining from CK19 or from NKp46 to determine the total tissue area.

For 3D image analysis, we used Imaris (Oxford Instruments). Cuboid volume was determined by creating a surface with the DAPI channel or background from another channel. CD31 and CD45 surfaces were created using Labkit for machine learning. For CD31, we applied a gaussian blur before further analysis. We trained the classifiers for d0 and d2 separately on a stack of two cuboids initially then applied the classifier to all of the cuboids in that day's group. For CD45 we trained the classifier on day 0 then applied those settings to all of the cuboids.

Cytokine analysis

For Py8119, cytokines tested in order were G-CSF, GM-CSF, IFNg, IL-1α, IL-1b, IL-2, IL-6, IL-12p40, IL-12p70, CXCL10, Lix, MIP-1α, MIP-1b, RANTES, and TNFα. For MC38..

Statistical analysis

Graphpad Prism 7 was used for statistics unless otherwise noted. Power analysis was performed using the average and standard deviation from the control conditions. https://clincalc.com/stats/samplesize.aspx

RPPA

Protein microarrays were printed and processed as previously described. Briefly, cuboid lysates (duplicates of 10 cuboids/sample) from the PY8119 syngeneic mouse breast adenocarcinoma cell line were prepared in 2% SDS lysis buffer (stock recipe (pH = 6.8): Tris·HCl 50 mM, 2% SDS, 5% glycerol, EDTA 5 mM, and NaF 1 mM. Then immediately before use, add protease inhibitors 1X, phosphatase inhibitors 1X, β-GP 10mM, PMSF 1 mM, Na_3VO_4 1 mM, and DTT 1 mM) and then printed onto RPPA slides, each containing 16 nitrocellulose pads (Grace Biolabs, GBL505116), using Aushon 2470 microarrayer (Aushon BioSystems). Samples were printed in duplicate and stored at −20 °C until processing. Slides were then washed with 1 M Tris·HCl (pH 9.0) for 2 to 3 days to remove SDS and PBS solution for 10 to 15 min, centrifuged with Thermo Sorvall Legend XTR Refrigerated Centrifuge (Thermo Scientific), and scanned with InnoScan 910 AL (Innopsys) to ensure no residual SDS. Slides were washed with PBS solution 2 to 3 times for 5 min each and then blocked with Odyssey blocking buffer (OBB) (Licor, 927–40000) for 1 hr at room temperature. Afterwards, slides were fitted to hybridization chamber cassettes (Gel Company, AHF16), incubated with primary antibodies on a shaker overnight at 4 °C. The following day, slides were washed with PBS thrice for 10 min each, blocked again with Odyssey blocking buffer (OBB) (Licor, 927–40000), and incubated with IRDye-labeled secondary antibodies for 1 hr at room temperature. After incubation, slides were washed in PBS 3 times for 10 min each, centrifuged again with Thermo Sorvall Legend XTR Refrigerated Centrifuge (Thermo Scientific), and scanned using Licor Odyssey CLx Scanner (LiCOR). Total signal intensity was normalized to total beta-actin (Sigma, Catalogue No A1978) and quantified using Array-Pro analyzer software package (Media Cybernetics, Maryland, USA).

Cuboid sample preparation for mass spectrometry analysis

4 PBS washed cuboids per replicate were resuspended in 40 µL of lysis buffer (6M GuHCL, 50 mM Tris pH 8.2, 75 mM NaCl, 10 mM TCEP, 30 mM CAA). The cuboid suspension was subjected to 4 rounds of agitation at 90 °C for 5 min followed by 15 min of bath sonication at 40 °C. Alkylation was quenched with 15 mM DTT for 30 min at RT and the samples were diluted 5-fold with Tris 50mM pH 8.9 prior to digestion, which was carried out overnight at 37°C using LysC at a 5ng/µL concentration. Digestion was quenched with 1% TFA prior to desalting with oasis prime HLB µElution (Waters). Desalted peptides were dried down by vacuum centrifugation.

Mass spectrometry data acquisition

Lyophilized peptide samples were resuspended in 3% ACN, 5% formic acid and subjected to liquid chromatography coupled to tandem mass spectrometry (LC-MS/MS). Samples were loaded into a 100 µm ID x 3 cm precolumn packed with Reprosil C18 1.9 µm, 120 Å particles (Dr. Maisch). Peptides were eluted over a 100 µm ID x 30 cm analytical column packed with the same material housed in a column heater set to 50°C and separated by gradient elution of 6 to 38% B (A: 0.15% FA , B: ACN 80% and 0.15% FA) over 65 min and 38% to 50% B over 8 min at 400 nL/min delivered by an Easy1200 nLC system (Thermo Fisher Scientific) with a total 90 min method length. Peptides were online analyzed on an Orbitrap Eclipse Tribrid mass spectrometer (Thermo Fisher Scientific). Mass spectra were collected using a data independent acquisition method. For each cycle a full MS scan (358-1100 m/z, resolution 60,000, and Standard 100% normalized AGC target in automatic maximum injection time mode) followed by 30 consecutive non-overlapping MS/MS scans with 24 m/z wide isolation windows. MS/MS scans were acquired at 30,000 resolution in centroid mode, using HCD fragmentation with 33% normalized collision energy and an 800% normalized AGC target with automatic maximum injection time mode. In alternating cycles, the mass target list for MS/MS scans was offset by 12 m/z to produce DIA windows with half overlap spanning the 363-1095m/z mass range.

Mass spectrometry Data Analysis

Raw files were converted to mzML format and demultiplexed using MSConvert followed by analysis with FragPipe (version 19.1) proteomics pipeline. Searches were performed with MSFragger (version 3.7) using a target/decoy *Mus Musculus* database (Uniprot fasta proteome: UP000000589_2023-03-02). Search parameters were set to 20 ppm for both precursor and fragment tolerances. LysC was selected as the digestive enzyme with a maximum of 1 missed cleavage and fixed constant carbamidomethylation modification of cysteines (+57.0215 Da) and variable modifications of methionine oxidation (+15.9949 Da) and protein N-terminal acetylation (+42.0106 Da). Search results were post-processed with Philosopher (version 4.8.1) using Percolator (3.05) filter the results to 1% FDR and ProteinProphet for protein inference. EasyPQP was used to generate a peptide spectral library and quantification was carried out using DIA-NN 1.8.2.

Bioinformatic analysis was performed using R (https://www.r-project.org/) and the R Studio environment. MSStats (version 4.01) was used to parse DIA-NN quantification outputs, generate and normalize protein quantification and carry out statistical significance analysis. Gene ontology enrichment analysis was carried out using CusterProfiler.

Author contributions

L.F.H., R.R-M, and T.G. designed, performed, and analyzed experiments and wrote the paper. S.L./M.Y performed and analyzed experiments. N.G. and I.S. performed experiments. C.S. analyzed experiments. R.Y. designed experiments. A.F. and J.V. designed and analyzed experiments, and wrote the paper.

Data availability

Multi-IHC images and 3D imaging data and analysis is available on request.

Conflicts of interest

L.F.H. and A.F. are the founders of OncoFluidics, a startup that seeks to commercialize microfluidic drug tests using intact tissues.

Acknowledgements

This work was supported by National Cancer Institute grants R21CA251952, R01 CA181445, and R01 CA272677. This work was also funded in part by ….for X. We thank Heidi Kenerson for preparation of human slices.

REFERENCES

1. Hanahan, D. & Coussens, L. M. Accessories to the Crime: Functions of Cells Recruited to the Tumor Microenvironment. *Cancer Cell* **21**, 309–322 (2012).
2. Jin, M. Z. *et al.* Organoids: An intermediate modeling platform in precision oncology. *Cancer Lett.* **414**, 174–180 (2018).
3. Ghaemmaghami, A. M., Hancock, M. J., Harrington, H., Kaji, H. & Khademhosseini, A. Biomimetic tissues on a chip for drug discovery. *Drug Discov. Today* **17**, 173–181 (2012).
4. Sontheimer-Phelps, A., Hassell, B. A. & Ingber, D. E. Modelling cancer in microfluidic human organs-on-chips. *Nat. Rev. Cancer* **19**, 65–81 (2019).

5. Li, X. *et al.* Navigating metabolic pathways to enhance antitumour immunity and immunotherapy. *Nat. Rev. Clin. Oncol.* **16**, 425–441 (2019).
6. Dougan, M., Dranoff, G. & Dougan, S. K. Cancer Immunotherapy: Beyond Checkpoint Blockade. *Annu. Rev. Cancer Biol.* **3**, 55–75 (2019).
7. Kruger, S. *et al.* Advances in cancer immunotherapy 2019 – latest trends. *J. Exp. Clin. Cancer Res.* **38**, 268 (2019).
8. Letai, A. Functional precision cancer medicine—moving beyond pure genomics. *Nat. Med.* **23**, 1028–1035 (2017).
9. Murciano-Goroff, Y. R., Warner, A. B. & Wolchok, J. D. The future of cancer immunotherapy: microenvironment-targeting combinations. *Cell Res.* **30**, 507–519 (2020).
10. Wong, C. H., Siah, K. W. & Lo, A. W. Estimation of clinical trial success rates and related parameters. *Biostatistics* **20**, 273–286 (2019).
11. Harrison, R. K. Phase II and phase III failures: 2013–2015. *Nat. Rev. Drug Discov.* **15**, 817–818 (2016).
12. Wouters, O. J., McKee, M. & Luyten, J. Estimated Research and Development Investment Needed to Bring a New Medicine to Market, 2009-2018. *J. Am. Med. Assoc.* **323**, 844–853 (2020).
13. Xin Yu, J. *et al.* Trends in clinical development for PD-1/PD-L1 inhibitors. *Nat. Rev. Drug Discov.* **19**, 163–164 (2020).
14. Jonas, O. *et al.* An implantable microdevice to perform high-throughput in vivo drug sensitivity testing in tumors. *Sci. Transl. Med.* **7**, 284ra57 (2015).
15. Klinghoffer, R. A. *et al.* A technology platform to assess multiple cancer agents simultaneously within a patient's tumor. *Sci. Transl. Med.* **7**, 284ra58-284ra58 (2015).
16. Wang, M. *et al.* Humanized mice in studying efficacy and mechanisms of PD-1-targeted cancer immunotherapy. *FASEB J.* **32**, 1537–1549 (2018).
17. Franko, A. J. & Koch, C. J. Binding of misonidazole to V79 spheroids and fragments of dunning rat prostatic and human colon carcinomas in vitro: Diffusion of oxygen and reactive metabolites. *Int. J. Radiat. Oncol. Biol. Phys.* **10**, 1333–1336 (1984).
18. Evans, S. M., Jenkins, W. T., Joiner, B., Lord, E. M. & Koch, C. J. 2-Nitroimidazole (EF5) binding predicts radiation resistance in individual 9L s.c. tumors. *Cancer Res.* **56**, 405–411 (1996).
19. Lao, Z. *et al.* Improved methods to generate spheroid cultures from tumor cells, tumor cells & fibroblasts or tumor-fragments: microenvironment, microvesicles and MiRNA. *PLoS One* **10**, e0133895 (2015).
20. Ricciardelli, C. *et al.* Novel ex vivo ovarian cancer tissue explant assay for prediction of chemosensitivity and response to novel therapeutics. *Cancer Lett.* **421**, 51–58 (2018).
21. Pirnia, F. *et al.* Ex vivo assessment of chemotherapy-induced apoptosis and associated molecular changes in patient tumor samples. *Anticancer Res.* **26**, 1765–1772 (2006).
22. Aref, A. R. *et al.* Screening therapeutic EMT blocking agents in a three-dimensional microenvironment. *Integr. Biol.* **5**, 381–389 (2013).
23. Aref, A. R. *et al.* 3D microfluidic: Ex vivo culture of organotypic tumor spheroids to model immune checkpoint blockade. *Lab Chip* **18**, 3129–3143 (2018).
24. Jenkins, R. W. *et al.* Ex vivo profiling of PD-1 blockade using organotypic tumor spheroids. *Cancer Discov.* **8**, 196–215 (2018).
25. Ootani, A. *et al.* Sustained in vitro intestinal epithelial culture within a Wnt-dependent stem cell niche. *Nat. Med.* **15**, 701–706 (2009).
26. Li, X. *et al.* Oncogenic transformation of diverse gastrointestinal tissues in primary organoid culture. *Nat. Med.* **20**, 769–777 (2014).
27. Boehm, J. S. *et al.* Organoid Modeling of the Tumor Immune Microenvironment. *Cell* **175**, 1972-1988.e16 (2018).

28. Astolfi, M. *et al.* Micro-dissected tumor tissues on chip: an ex vivo method for drug testing and personalized therapy. *Lab Chip* **16**, 312–325 (2016).
29. Chatzidimitriou, F. A Platform to Restore Intra-Tissue Flow in Live Explant Assays. *Ph.D. thesis, Imperial College London (Bioengineering Department)* (2021). Available at: https://doi.org/10.25560/100935.
30. Crosby, D. *et al.* Early detection of cancer. *Science* **375**, 1244 (2022).
31. Horowitz, L. F. *et al.* Microdissected "cuboids" for microfluidic drug testing of intact tissues. *Lab Chip* **21**, 122 (2021).
32. Groebe, K. & Mueller-Klieser, W. On the relation between size of necrosis and diameter of tumor spheroids. *Int. J. Radiat. Oncol.* **34**, 395–401 (1996).
33. Sivakumar, R. *et al.* Organotypic tumor slice cultures provide a versatile platform for immuno-oncology and drug discovery. *Oncoimmunology* **8**, e1670019 (2019).
34. Horowitz, L. F. *et al.* Multiplexed drug testing of tumor slices using a microfluidic platform. *Nat. Precis. Oncol.* **4**, 12 (2020).
35. Bazzichetto, C. *et al.* Interleukin-8 in Colorectal Cancer: A Systematic Review and Meta-Analysis of Its Potential Role as a Prognostic Biomarker. *Biomedicines* **10**, 2631 (2022).
36. Itatani, Y. *et al.* The Role of Chemokines in Promoting Colorectal Cancer Invasion/Metastasis. *Int. J. Mol. Sci.* **17**, 643 (2016).
37. NCI. Colon Cancer Treatment (PDQ®)–Health Professional Version. *Cancer.gov* (2024). Available at: https://www.cancer.gov/types/colorectal/hp/colon-treatment-pdq.
38. Morris, V. K. *et al.* Treatment of Metastatic Colorectal Cancer: ASCO Guideline. *J. Clin. Oncol.* **41**, 678–700 (2023).
39. Li, W., Germain, R. N. & Gerner, M. Y. High-dimensional cell-level analysis of tissues with Ce3D multiplex volume imaging. *Nat. Protoc.* **14**, 1708–1733 (2019).
40. Schindelin, J. *et al.* Fiji: An open-source platform for biological-image analysis. *Nat. Methods* **9**, 676–682 (2012).

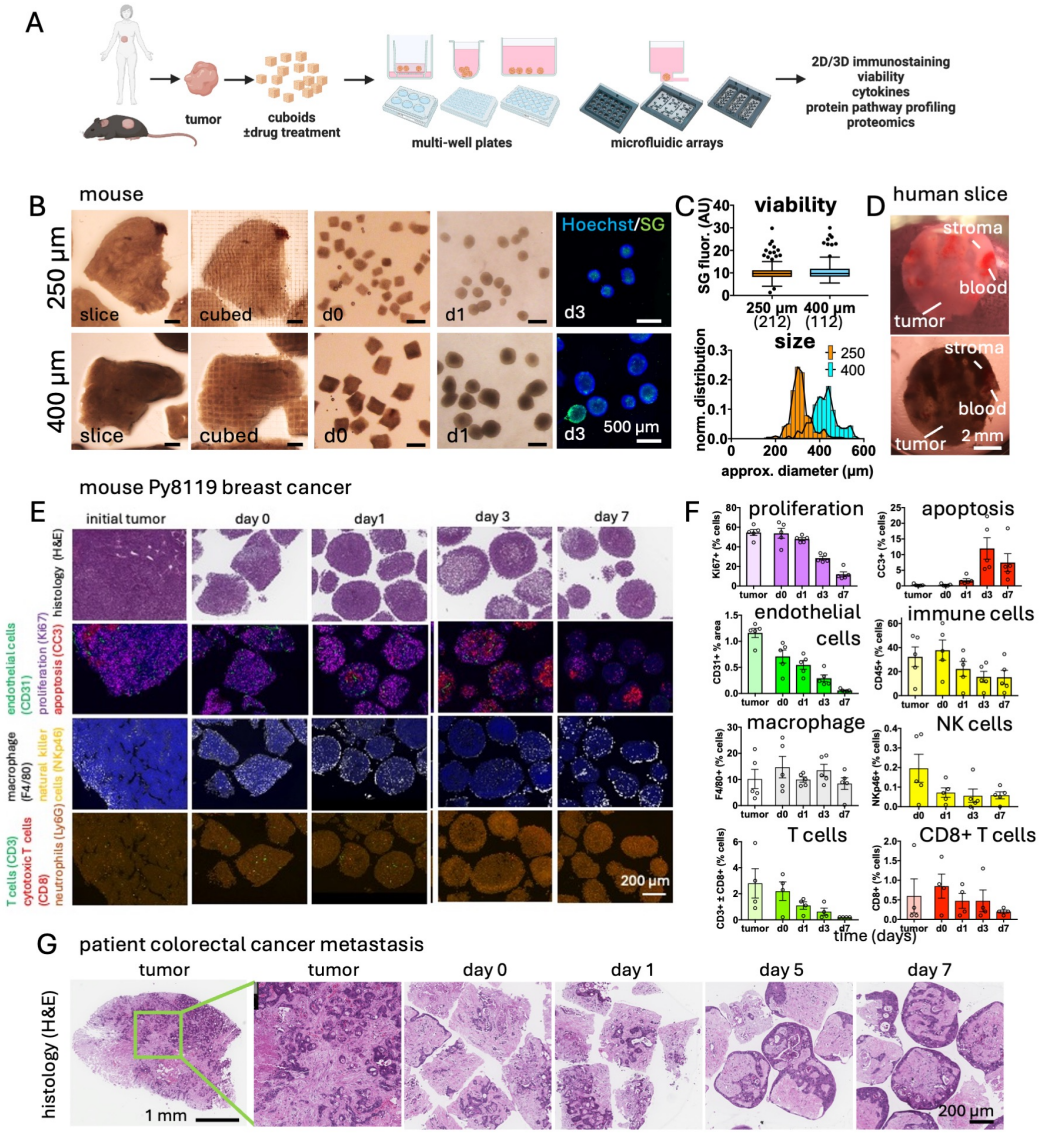

Figure 1: Cuboid generation and culture. (**A**) Schematic of cuboid workflow. (**B**) Sequential formation and culture of 250 or 400 µm mouse Py8119 breast cancer syngeneic tumor cuboids, with vibratome sectioning to make slices, tissue chopper to make polygonal cuboids (day 0), and spherical morphology at day 1 and day 3. Viability was assessed at day 3 using the SYTOX green dye (SG) for dead nuclei and the Hoechst blue dye for all nuclei. Cuboids were cultured in 6-well plates. (**C**) Graphs of viability (Tukey whisker plot) and size (histogram) of cuboids at day 3. (**D**) Patient colorectal cancer liver metastasis (CRCm) slice visualized with either top illumination or through illumination (bottom). (**E,F**) Histology and fluorescent multi-immunohistochemistry (multi-IHC) of mouse Py8119 breast cancer cuboids grown in a 6-well plate. (**E**) Histology (H&E), multi-IHC for endothelial cells (CD31), cell death (cleaved-caspase 3, CC3), and proliferation (Ki67); and multi-IHC for immune cell subtypes with macrophage (F4/80, *Adgre1*), NK cells (NKp46, scarce), T cells (CD3), and cytotoxic T cells (CD8) and neutrophils (Ly6G, weak stain). (**F**) Quantitation of cell staining in (**E**). (**G**) H&E histology of a patient colorectal cancer liver metastasis, showing the initial tumor and cuboids taken before or after culture in a 6-well plate.

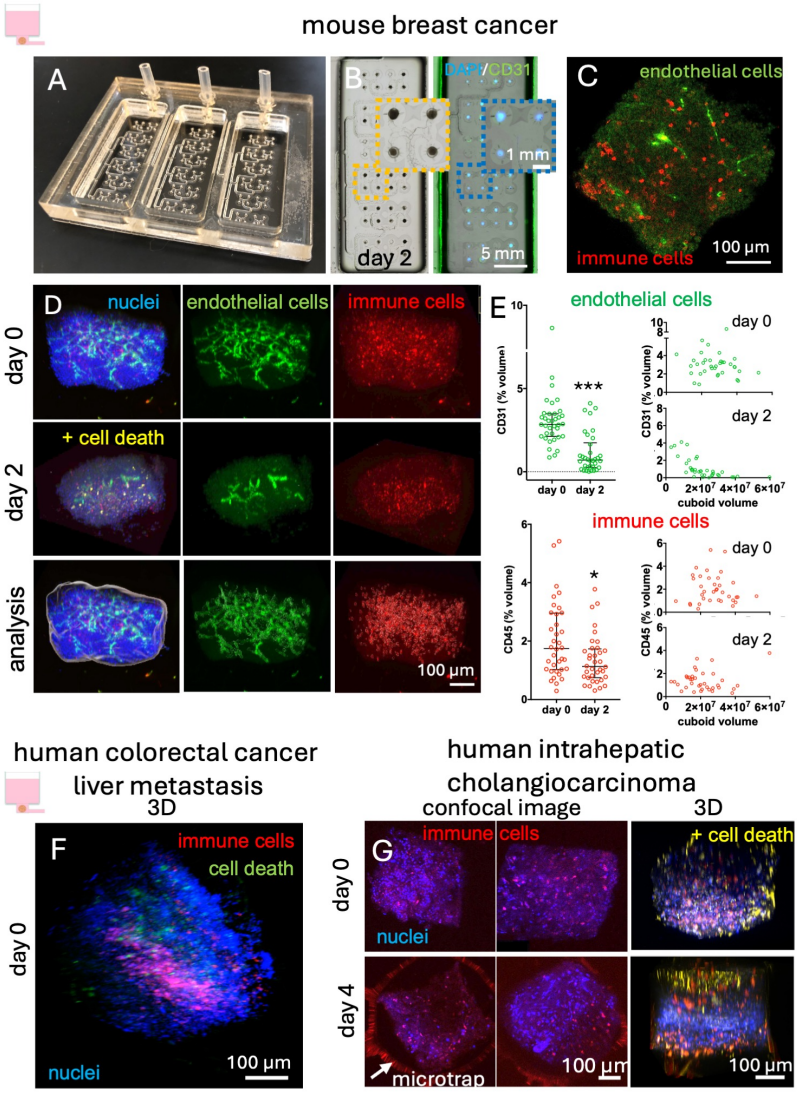

Figure 2. Heterogeneity of TME by 3D imaging. (A) Microfluidic device used for on-device immunostaining, clearing, and confocal imaging. 3 independent wells each have 48 cuboid traps each connected by binaries to 1 output. (B-E) 3D imaging and analysis of mouse Py8119 cuboids. (B) One well showing Py8119 mouse cuboids in the device after 2 days in culture, and then after immunostaining (CD31 for endothelial cells, CD45 for immune cells, cleaved-caspase-3 for cell death, DAPI nuclear stain), and clearing with Ce3D. (D) Confocal image of immunostaining for day 0 and day 5 cuboid with Imaris 3D analysis underneath. (E) Graphs showing quantitation of endothelial and immune cell staining for individual cuboids (points). Median and quartile bars in black. n=34-36 cuboids. Mann-Whitney test. *p<0.05, ***P<0.0001. (F) 3D Imaris image from confocal images of a cuboid from a patient colorectal cancer liver metastasis after 3D immunostaining with CD45 for immune cells, cleaved-caspase-3 for cell death, and a DAPI nuclear stain. (G) 3D confocal and 3D Imaris images of cuboids from a patient idiopathic cholangiocarcinoma (ICC) both at day 0 or after 4 days culture in the microfluidic device.

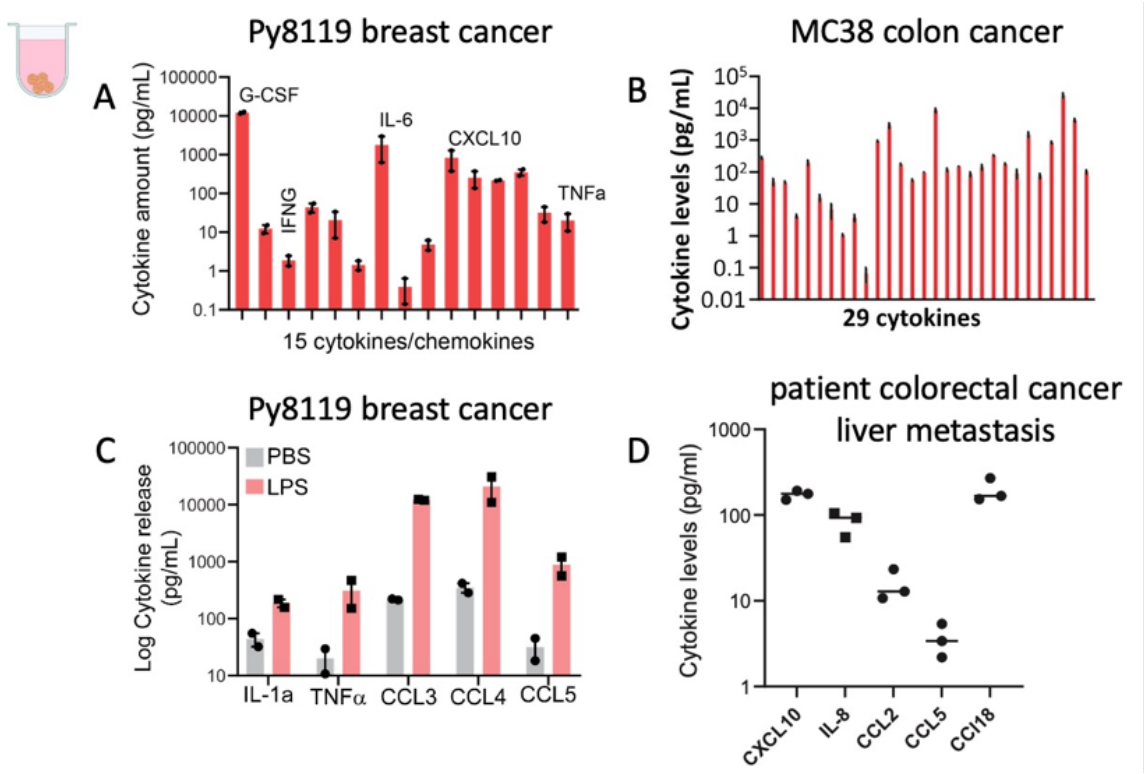

Figure 3. Immune cell-dependent responses in cuboids in a 96-well plate. Cytokine/chemokine secretion in cuboids grown in 96 well plates, measured by Luminex. (A) Baseline secretion from Py8119 mouse breast cancer cuboids (15 of 31 cytokines, 2-6 cuboids/well). (B) Baseline secretion from MC38 mouse colon cancer cuboids (29 cytokines, 4-8 cuboids/well). (C) Cytokine response of Py8119 cuboids to LPS stimulation (2-6 cuboids/well). (D) Baseline secretion from human colorectal cancer metastasis cuboids (4-6 cuboids per well, day 5). Individual replicates shown.

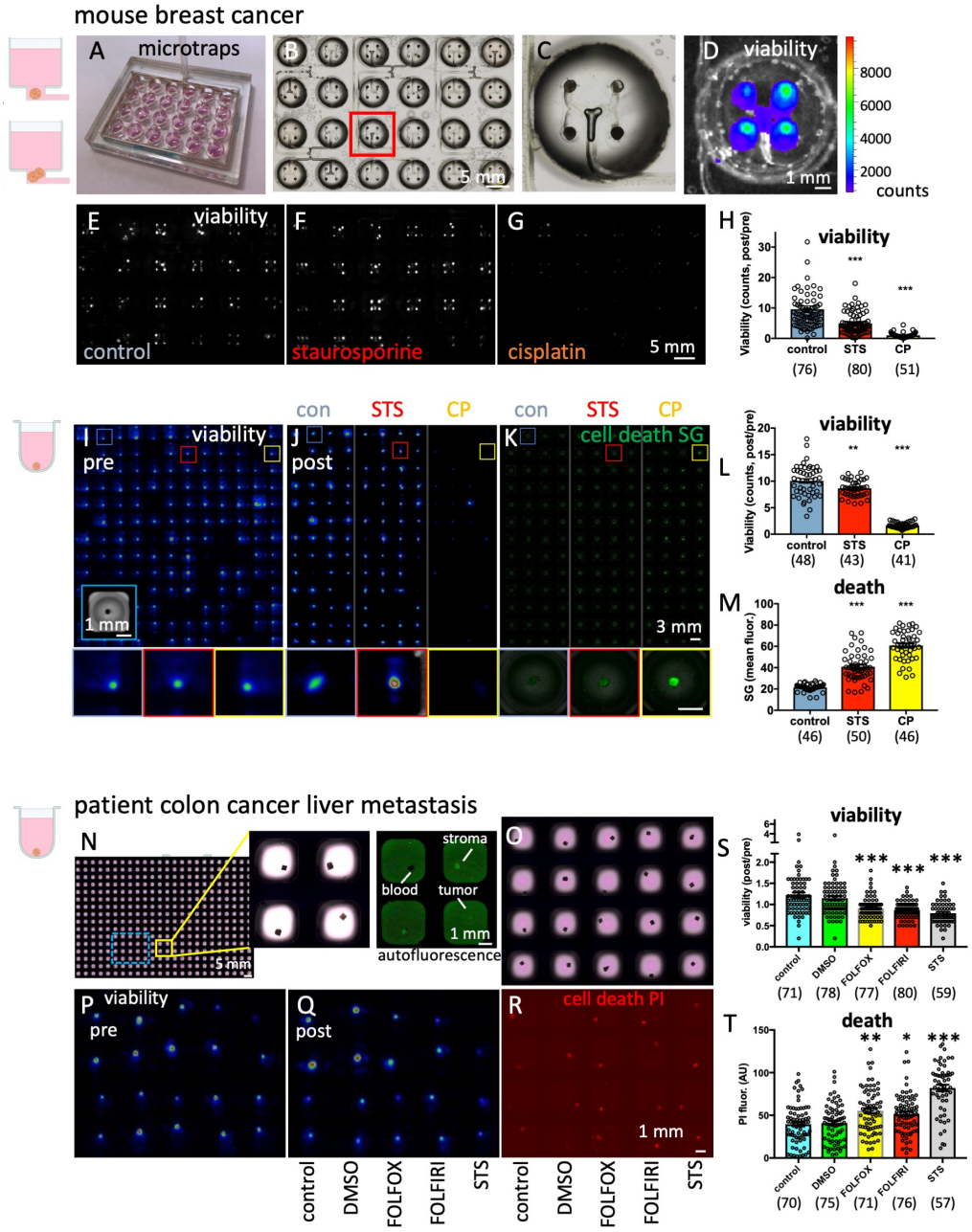

Figure 4. Drug treatment of mouse and human tumor cuboids. Py8119 mouse breast cancer cuboids were treated in parallel either on a microfluidic device (A-H) or with individual cuboids in a 384-well plate (I-M). (A) Microfluidic device with 24 wells, 4 traps/well. (B-D) Py8119 mouse breast cancer cuboids loaded on a device (B, C closeup) with viability by RealTime-Glo luminescence imaging (D). (E-G) Viability after 3 days drug treatment of 3 different devices with staurosporine (STS, 2 µM) or cisplatin (CP, 100 µM). (H) Graph shows changes in viability by luminescence for individual traps (1-3 cuboids each trap). Ave ± sem. Kruskal Wallace test versus control with Dunns multiple comparisons. ***p<0.001. (I-K) Drug responses of individual cuboids, manually pipetted to have one per well on a 384-well plate, measured for viability by RealTime-Glo luminescence (I,J) and for cell death by SYTOX green (SG) nuclear stain (K). Close-ups

shown below. (L,M) Graphs of viability and cell death, with responses of individual cuboids (circles) and ave ± sem. One way ANOVA, Tukey post-hoc. ***$p<0.0005$. N=41-50. (N-T) Drug treatment of human colorectal cancer liver metastasis cuboids, transferred by a robot to a 384-well plate (N), with 1 cuboid per well and closeups of yellow region showing heterogeneity revealed by green autofluorescence. After exposure to drugs for 5 days, viability was measured by RTG luminescence and death was measured by propidium iodide (PI). (O-R) Closeups of blue rectangle in (N). (P) Pre-treatment viability with RealTime-Glo on day 3. (Q) Post-treatment viability at day 7. (R) Cell death by propidium iodide staining on day 7. (S) Graph of viability by RTG with post/pre for each cuboid. (T) Graph of cell death by PI. Responses of individual cuboids (circles) and average ± sem. Student T-test (ANOVA pending). 8 wells with two cuboids per well not included. DMSO (0.2%). FOLFOX (1 µg/mL 5-fluorouracil, 1 µg/mL oxaliplatin). FOLFIRI (1 µg/mL 5-fluorouracil, 2 µg/mL irinotecan), STS (staurosporine 1 µM). Ave ± sem. Kruskal-Wallis test with Dunn's multiple comparisons versus DMSO. *$p<0.05$. **$p<0.01$. ***$p<0.0005$.

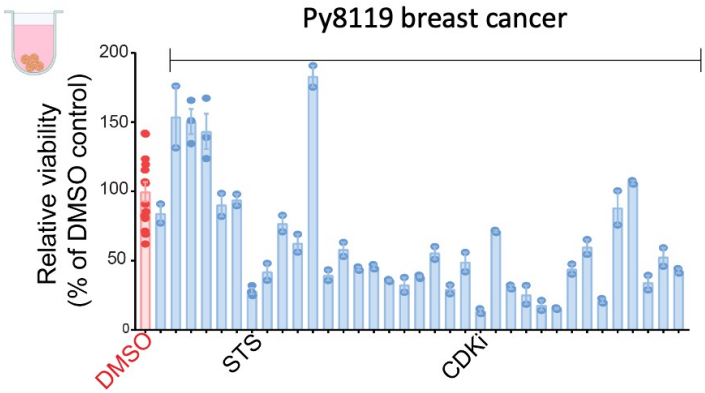

Figure 5. Responses of mouse and human cuboids to drug panels. Responses of mouse Py8119 cuboids to a panel of kinase inhibitors (1 µM). Viability measured by RealTime-Glo before and after 3 day treatment with drug panels as compared to DMSO control. Duplicates. N=2-6 cuboids/well and 34 kinase inhibitors. Staurosporine (STS) and non-specific kinase inhibitor (CDKi) positive controls.

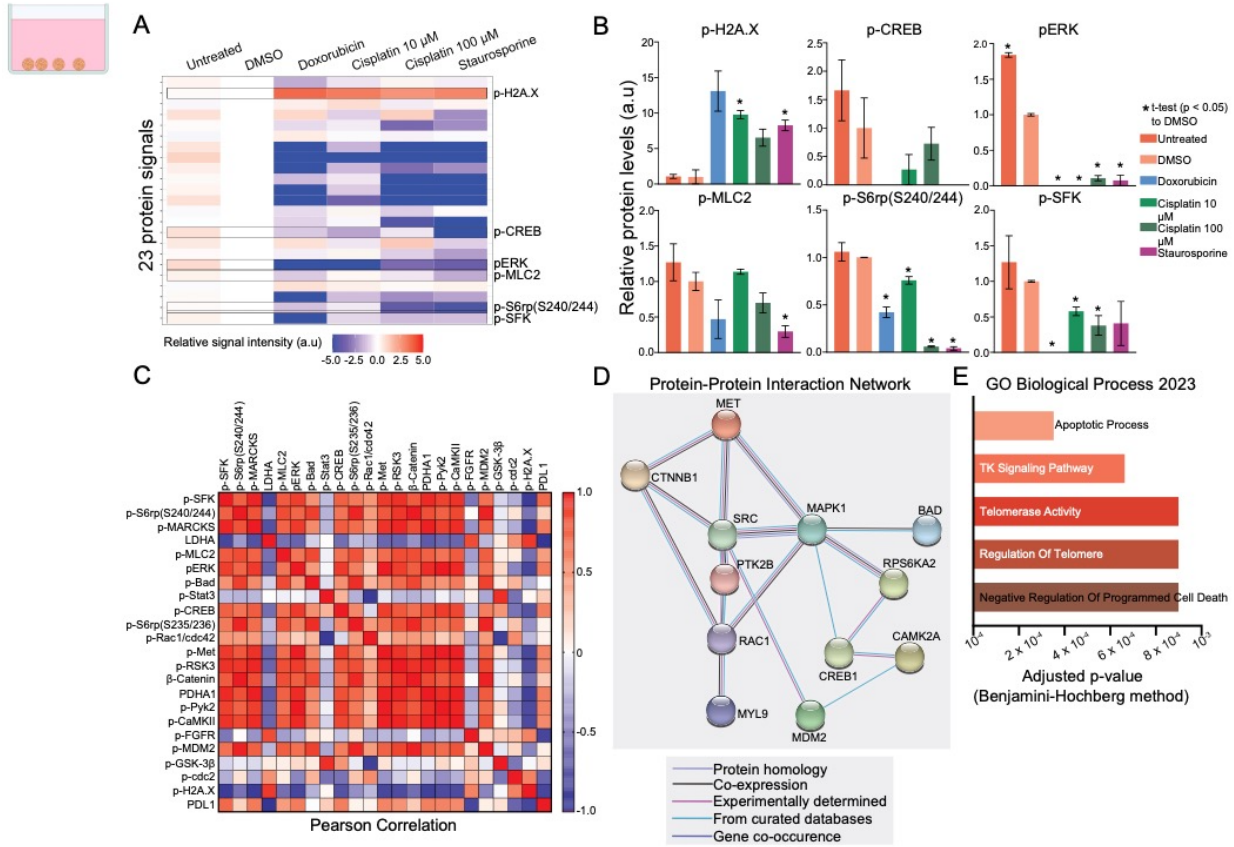

Figure 6. Profiling changes in signaling pathways from drug treated PY8119 breast cuboids. Reverse-phase protein array (RPPA) was used to profile 48 proteins from PY8119 breast cuboid samples after treatment for 3 days (untreated, 0.1% DMSO, Doxorubicin 10 µM, Cisplatin 10 µM, Cisplatin 100 µM, or Staurosporine 2 µM). Data from the 23 high-quality signals are shown. (A) Heatmap representation of relative signal intensities, normalized in a stepwise manner: beta-actin levels, untreated samples, and DMSO treated samples. (B) Graphical representation of relative protein levels from annotated proteins in (A), normalized in the same process as in (A) except without log2 transformation. *$p < 0.05$ unpaired t-tests compared to DMSO. (C) Pearson Correlation. The correlation matrix depicts the result of a Pearson correlation analysis performed on the 23 proteins of interest using measurements taken from all samples. (D) Protein-protein interaction network from positively correlated proteins in (C) (StringDB). (E) Gene enrichment analysis using the same positively correlated proteins from (C) (Enrichr). Adjusted p-values corrected for multiple hypothesis testing by the Benjamini-Hochberg method. Full names of top biological processes: regulation of apoptotic process, transmembrane receptor protein tyrosine kinase signaling pathway, regulation of telomerase activity, and regulation of telomere maintenance via telomerase.

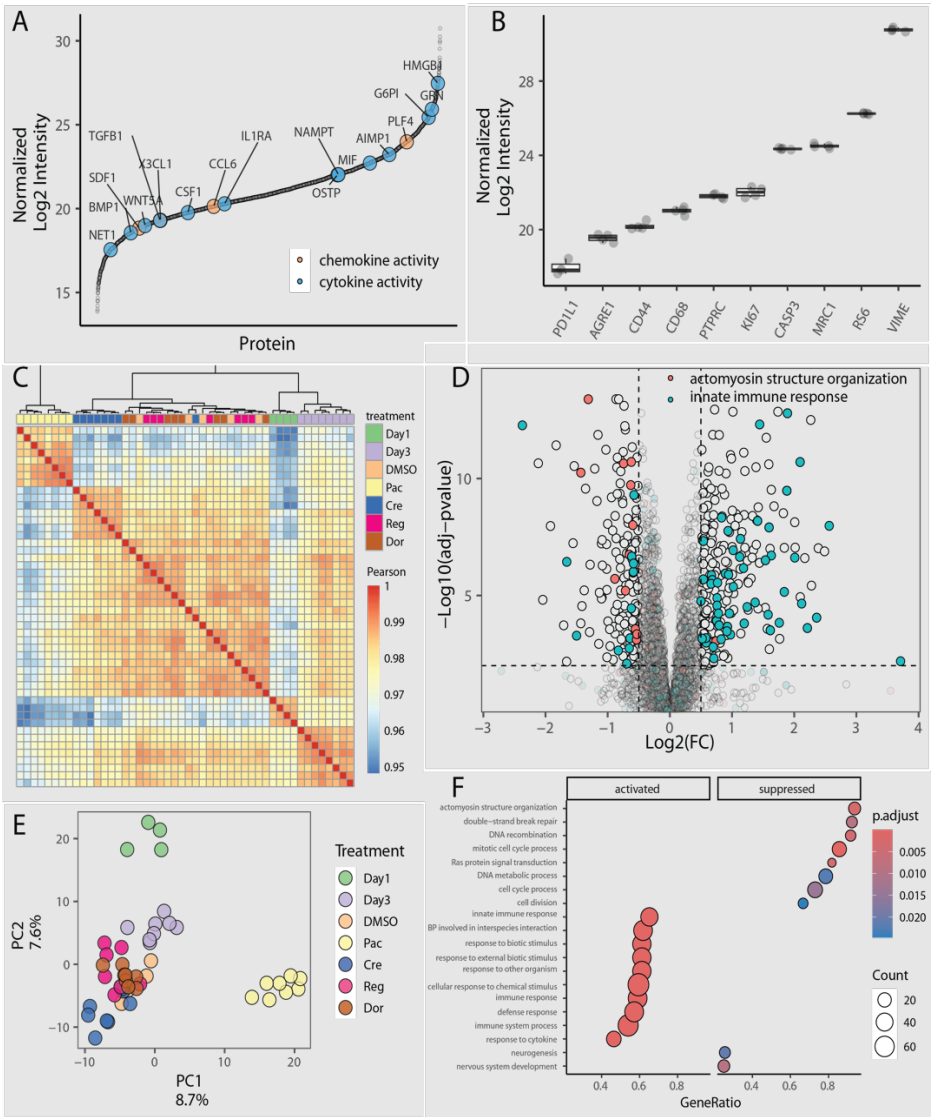

Figure 7. Profiling PY8119 breast cuboid proteomes using mass spectrometry and its changes upon drug treatments. Quantification of TME proteins: **A)** Ranked plot for median normalized log2 protein intensities in Day1 samples; highlighted proteins associated with GO terms: chemokine (yellow) and cytokine activites (blue). **B)** Box and Dot plot of Day 1 normalized protein log2 intensities for observed TME markers. Observed changes to the cuboid proteome upon drug treatment. **C)** Heatmap: Pearson correlations for protein abundances across drug treatments and replicates. (Day1, Day3: 0.5 untreated-day 3, **DMSO**: 0.1% DMSO-day 3, **Pac**: 10 µM paclitaxel-day 3, **Cre**: 0.5 µM crenolanib-day 3, **Reg**: µM regorafenib-day 3, **Dor**: 0.5 µM doramapimod-day3). **E)** Dot plot: PC1 and PC2 of principal component analysis for protein abundance measurements across treatments and replicates. **D)** Volcano plot: protein abundance log2 fold changes between DMSO and Paclitaxel treatments on day 3 and adjusted p-values. Log2 fold changes and multiple hypothesis testing adjusted p-values were calculated using MSStats linear model. Highlighted proteins in (**grey**) with fold change threshold |Log2FC| > 0.5 and adjusted p-value<0.01; associated with Gene Ontology terms: (**blue**) innate immune response, (**red)** actomyosin structure organization. **F)** Gene Ontology enrichment analysis of Biological Process terms for upregulated and downregulated proteins between DMSO and Paclitaxel treatments.